coatings

Article

Periodically Sinusoidal Magnetic Stray Field and Improved Film Quality of CoMnP Micro-Magnet Arrays for Magnetic Encoders by Electrodeposition with the Assistance of Ultrasound

Geng-Hua Xu [1], Jung-Yen Chang [1], Hsiang-Chun Hsueh [2] and Chiao-Chi Lin [1,*]

[1] Department of Materials Science and Engineering, Feng Chia University, Taichung 40724, Taiwan
[2] Micro/Meso Mechanical Manufacturing R&D Department, Metal Industries Research & Development Centre (MIRDC), Kaohsiung 81160, Taiwan; hchsueh@mail.mirdc.org.tw
* Correspondence: chiaochi@fcu.edu.tw

Abstract: Magnetic encoders are composed of a magnetic sensor, a hard magnetic recording medium and a signal processing circuit. Electrodeposited micro-magnet arrays produced by micro-fabrication are promising recording media for enhancing encoder performance. However, two major engineering issues have yet to be resolved. One issue is an unknown relationship between the feature sizes of micro-magnet arrays and their stray field shapes, and another issue is the formation of micro-cracks due to the built-up residual stresses of thick films. In this study, we investigated the effect of feature sizes on the emanating stray field shape at various observation heights. Feature sizes include two height (i.e., film thickness) values of 78 μm and 176 μm, and both width and spacing with three values of 360 μm, 520 μm and 680 μm. Ultrasound-assisted agitation was adopted for investigating the effects of electrodepositing current densities on the film crystalline microstructures and magnetic properties. Narrowing the width of micro-magnets helps the stray field to become a sinusoidal profile. Thinner film, i.e., thickness 78 μm in this study, supports the stray field taking on a sinusoidal profile. Moreover, the spacing between the micro-magnets plays a key factor in determining the shape of the stray field. Under 37 kHz/156 W ultrasound agitation, the optimal hard magnetic properties of electrodeposited CoMnP films are residual magnetization 2329 G and coercivity 968 Oe by a current density of 10.0 mA/cm^2. Ultrasound-assisted electrodeposition, along with duly designed feature size, facilitates the micro-magnet arrays having a sinusoidal stray field shape using high quality films. Furthermore, for the first time, a systematic understanding of feature-size-dependent stray field evolution and improved polarities quality has been realized for the recording media of sinusoidal magnetic encoders.

Keywords: magnetic encoders; hard magnetic films; electrodeposition; ultrasound-assisted agitation; micro-fabrication; magnetization; micro-magnet arrays; feature sizes; magnetic stray field

check for updates

Citation: Xu, G.-H.; Chang, J.-Y.; Hsueh, H.-C.; Lin, C.-C. Periodically Sinusoidal Magnetic Stray Field and Improved Film Quality of CoMnP Micro-Magnet Arrays for Magnetic Encoders by Electrodeposition with the Assistance of Ultrasound. *Coatings* **2024**, *14*, 1340. https://doi.org/10.3390/coatings14101340

Academic Editor: Uta Klement

Received: 20 September 2024
Revised: 12 October 2024
Accepted: 18 October 2024
Published: 21 October 2024

1. Introduction

Magnetic encoders traditionally rely on hard magnetic ferrites for their recording media [1–4]. Rare-earth hard magnets such as SmCo by gas flow sputtering have also been considered [5]. However, these materials encounter limitations in achieving high storage densities, fine magnetic pole pitches and desired stray field waveforms, hindering the development of magnetic encoders with higher performance. Moreover, the fabrication methods of these materials involve sintering, bonding and vacuum-related processes, which require intricate designs for fabricating recording media on targeted workpieces.

Recording media adopted in the hard disks industry have demonstrated emerging potentials for realizing high-performance magnetic encoders [6–11]. Among them, electrodeposited Co-rich films offer numerous advantages, including high deposition rate, cost-effectiveness and tunable mechanical and magnetic properties [9–13]. Electrodeposited Co-rich films are crystalline, having a hexagonal close-packed (HCP) microstructure with an easy magnetization in the *c*-axis direction. Electrodeposition of the CoMnP alloy has a strong propensity for perpendicular anisotropy of Co-HCP (002) texture formation [14–17]. In addition, the electrodeposited Co-rich films can be deposited on various substrates such as aluminum alloys, steels and silicon wafers, making them suitable for integration into different encoder designs.

To enhance the resolution of magnetic encoders, Xu et al. illustrated the combination of micro-fabrication and CoNiP electrodeposition for producing micro-magnet arrays with periodical magnetic stray fields [10]. The micro-magnet arrays can be fully magnetized with a single pulse in a solenoid coil, resulting in sinusoidal and symmetrical stray field profile. Theis et al. further demonstrated an encoder accuracy of about ± 1 μm over a length of 2.5 cm using the recording media of electrodeposited CoP micro-magnet arrays [11]. The technique of fabricating micro-magnet arrays has been well-developed [18–24]. However, there is limited research showing the effect of feature sizes such as width, height and spacing of micro-magnet arrays on the resultant stray field shapes.

Furthermore, Ref. [11] indicates the challenge with electrodeposited Co-rich micro-magnets, which is reducing the inherent residual stress for thick film deposition so that micro-magnets with crack-free morphology and decent adhesion can be produced. Grapes et al. pointed out that electrolyte agitation is a key factor in reducing residual stress and preserving the hard magnetic properties of electrodeposited Co-rich thick (>10 μm) films [25]. On the other hand, inevitable hydrogen evolution due to cathodic reaction can lead to crater-like micro-pits when improper electrolyte agitation is conducted. Defective morphologies are adverse for the formation of periodically sinusoidal magnetic stray fields. Comparing with traditional mechanical agitation methods such as vibrating, rotating, paddling and stirring [26–28], conventional air-bubbling and ultrasound-assisted agitation methods are competent to debubble hydrogen during electrodepositing micro-magnets into photoresist (PR) arrays [28,29]. Based on the aforementioned points, this study aims to address the unclear relationship between feature sizes and stray field profiles, while improving the deposited film quality through ultrasound-assisted agitation of the electrolyte bath.

This work is divided into four main parts based on the research directions and experimental processes. The first part outlines the technology of magnetic encoders and their requirements of sinusoidal magnetic stray fields for improved performance. The second part investigates the influence of micro-magnet feature sizes on the shape and strength of stray fields. The micro-magnets were realized through combining micro-fabricated photoresist (PR) grating arrays and electrodepositing CoMnP hard magnetic alloy using air bubbling agitation, followed by a single-step (i.e., one-time) magnetization, as shown in Figure 1a. The third part focuses on reducing surface micro-cracks of CoMnP films through ultrasound-assisted electrodeposition, facilitating the investigation of electrodepositing current density effects on the quality of the CoMnP hard magnetic films, as depicted in Figure 1b. Note that current density dominates the depositing rate of an electrodeposition system according to Faraday's Law of electrolysis, and hence the present study adopts constant ultrasonic frequency and power values for investigating the effect of current densities. Finally, the fourth part integrates and optimizes the aforementioned two techniques. A two-step electrodepositing processes of air bubbling agitation and ultrasonic agitation to minimize surface micro-cracks on the fine pole pitch CoMnP micro-magnet arrays, which present a sinusoidal stray field profile, has been successfully realized (Figure 1c). This study majorly explores the effect of feature sizes of micro-magnet arrays and the current density of ultrasound-assisted electrodeposition on magnetic stray field shape and film quality for advancing novel recording media of magnetic encoders.

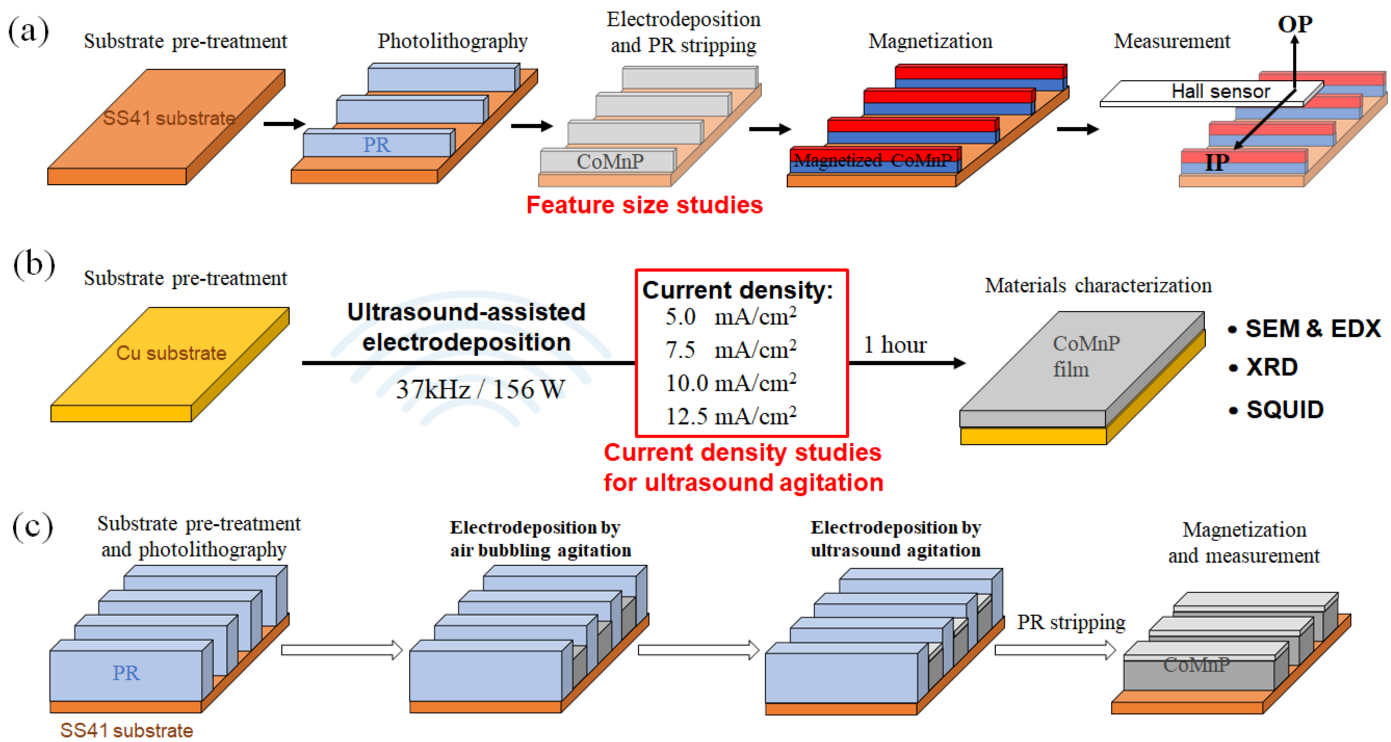

Figure 1. Schematic diagrams of three main parts of the present work: (**a**) The experimental process for the studies of micro-magnet feature sizes by micro-fabrication and electrodepositing processes using a low-carbon steel substrate with a thickness of 4.0 mm. (**b**) Studies of electrodepositing current density under ultrasound-assisted electrodeposition using a copper substrate with a thickness of 0.5 mm for investigating film quality and materials properties. (**c**) Integration and optimization of the techniques from (**a**,**b**) using a low-carbon steel substrate to realize fine pole pitch micro-magnet arrays with mitigated surface micro-cracks having a sinusoidal stray field.

2. Magnetic Encoders and Sinusoidal Stray Field

Magnetic encoders are key positioning systems in precision engineering for manufacture, automotive, aerospace and robotics. Considering sinusoidal encoders and comparing with optical encoders, magnetic encoders possess many advantages, including greater resistance to rugged environments such as dust, oil and splashing liquids [30]. The major components of a sinusoidal magnetic encoder are magneto-resistance (MR) sensors, hard magnetic recording media and signal processing circuitry. The performance of magnetic encoders is closely tied to the quality and characteristics of their recording media.

Through magnetization process, the recording medium forms periodically alternating north and south polarities, producing raw input signals as the MR sensor passes over the recording medium. The resolution and positioning accuracy of a magnetic encoder are determined by the quality of the magnetic stray field produced by the magnetic recording medium [31]. An ideal magnetic stray field is in the shape of a sinusoidal waveform [32–34]. The finer the pole pitch of the alternating north and south polarities is, the higher the resolution of the magnetic encoder. Therefore, fabricating hard magnetic recording media with fine pitch sinusoidal stray fields is crucial for high-performance magnetic encoders.

3. Materials and Methods

3.1. Micro-Fabrication and Electrodeposition of CoMnP Micro-Magnet Arrays and Films

3.1.1. Photolithography Process

The photolithography process was performed on SS41 low-carbon steel substrates with an effective area of 1.0 cm × 1.0 cm. The process consisted of five main steps: spin coating, soft baking, UV exposure, post-exposure baking (PEB) and development. The feature sizes involved in the mask design investigated two aspects in terms of varying width (W) and spacing (D) with two micro-magnet heights (H) of 78 µm and 176 µm (Table 1). Another mask design of W = 200 µm and D = 360 µm was used for the study of fine pole pitch micro-magnet arrays, i.e., the process shown in Figure 1c. All the masks were made of thin stainless-steel sheets through electrical discharge machining (EDM) with an error of ±5 µm.

Table 1. List and symbols of the feature sizes that are designed and studied in this work.

Micro-Magnet Height (Symbol)	Fixed Width (Varying Spacing) †	Fixed Spacing (Varying Width) †
176 µm (T)	W360-D360 W360-D520 W360-D680	W360-D360 W520-D360 W680-D360
78 µm (F)	W360-D360 W360-D520 W360-D680	W360-D360 W520-D360 W680-D360

† The numbers following W and D denote the width and spacing dimensions in micrometer, respectively.

In the photolithography process, a negative-type thick PR (NR26-25000P, Futurrex, Inc., Franklin, TN, USA) was applied using a two-step spin coating process. In the first step, the substrate was spinning at 700 rpm for 40 s to evenly distribute the PR. In the second step, the substrate was spinning at 1300 rpm for 12 s to remove excess PR and determine the PR thickness. A soft bake process of heating the sample at 150 °C for 450 s was then conducted.

Next, the thick PR on the samples was exposed in a UV exposure unit (KVB-30DQ, KINSTEN, Taipei City, Taiwan) with 2300 mJ/cm^2. After exposure, the sample was baked at 90 °C for 300 s to cure and enhance the stability of the PR. Finally, the sample was immersed in a developer solution (RD6, Futurrex, Inc., USA) for 720 s, with gentle agitation to remove the unexposed PR, leaving the PR pattern of grating micro-arrays. The uncovered substrate areas were then ready for the subsequent electrodeposition process.

3.1.2. Electrodeposition Process

Electrodeposition was performed in a 110 mL electrolyte bath (with formulation and parameters shown in Table 2) to obtain two different heights, 78 µm and 176 µm, of the micro-magnets. The current density was set to 5 mA/cm^2. For the study of feature size effect, an air pump was used for electrolyte agitation to ensure uniform distribution of the chemical species and removal of hydrogen bobbles.

Table 2. The electrolyte bath composition and depositing parameters for the electrodeposition of the CoMnP alloy.

Stoichiometry of Magnetic Alloy	Bath Composition	Concentration (Mole/L)
CoMnP	$CoCl_2{\cdot}6H_2O$ $CoSO_4{\cdot}7H_2O$ $MnCl_2{\cdot}4H_2O$ $NaH_2PO_2{\cdot}H_2O$ NH_4Cl	0.42 0.053 0.4 0.2 1.8
Electrodeposition Method	**Deposition Parameter**	**Setting**
Galvanic deposition	Bath volume pH value Current density (CD) Temperature	110 mL 3.7 5 mA/cm^2 25 °C

For the ultrasound-related study, electrodeposition was performed using copper substrates with a depositing area of 1.0 cm × 1.0 cm. The electrolyte solution was agitated using an ultrasonic machine (Elma-P30H, Elma Schmidbauer GmbH, Singen, Germany) and water bath with fixed ultrasonic conditions of 37 kHz/156 W. Four different current densities of 5.0 mA/cm^2, 7.5 mA/cm^2, 10.0 mA/cm^2 and 12.5 mA/cm^2 were studied, with a constant electrodeposition time of 1 h. To prevent temperature increases caused by ultrasonic vibrations, which could affect the electrodeposition results, two external circulation pumps were used to circulate and cool the water bath, maintaining the electrolyte solution at a constant temperature of 26 °C.

3.1.3. Magnetization

The samples were magnetized using an oil-based capacitive discharge pulse magnetizer (MD-2002-O-2, NEY HWU ELECTRICAL Co., Ltd., Taipei City, Taiwan) along with a C-shaped magnetizing head made of low-carbon steel (Figure 2a). The cross-sectional area of the magnetizing head is 1.1 cm × 1.1 cm. The head was wound with 64 turns of copper wire to form a solenoid. The top surfaces of CoMnP micro-magnets of the sample were tightly pressed to the upper yoke of the magnetizing head during magnetization. Applied field (Happ) in the OP direction of samples was generated by a voltage of 800 V set and produced in the magnetizer.

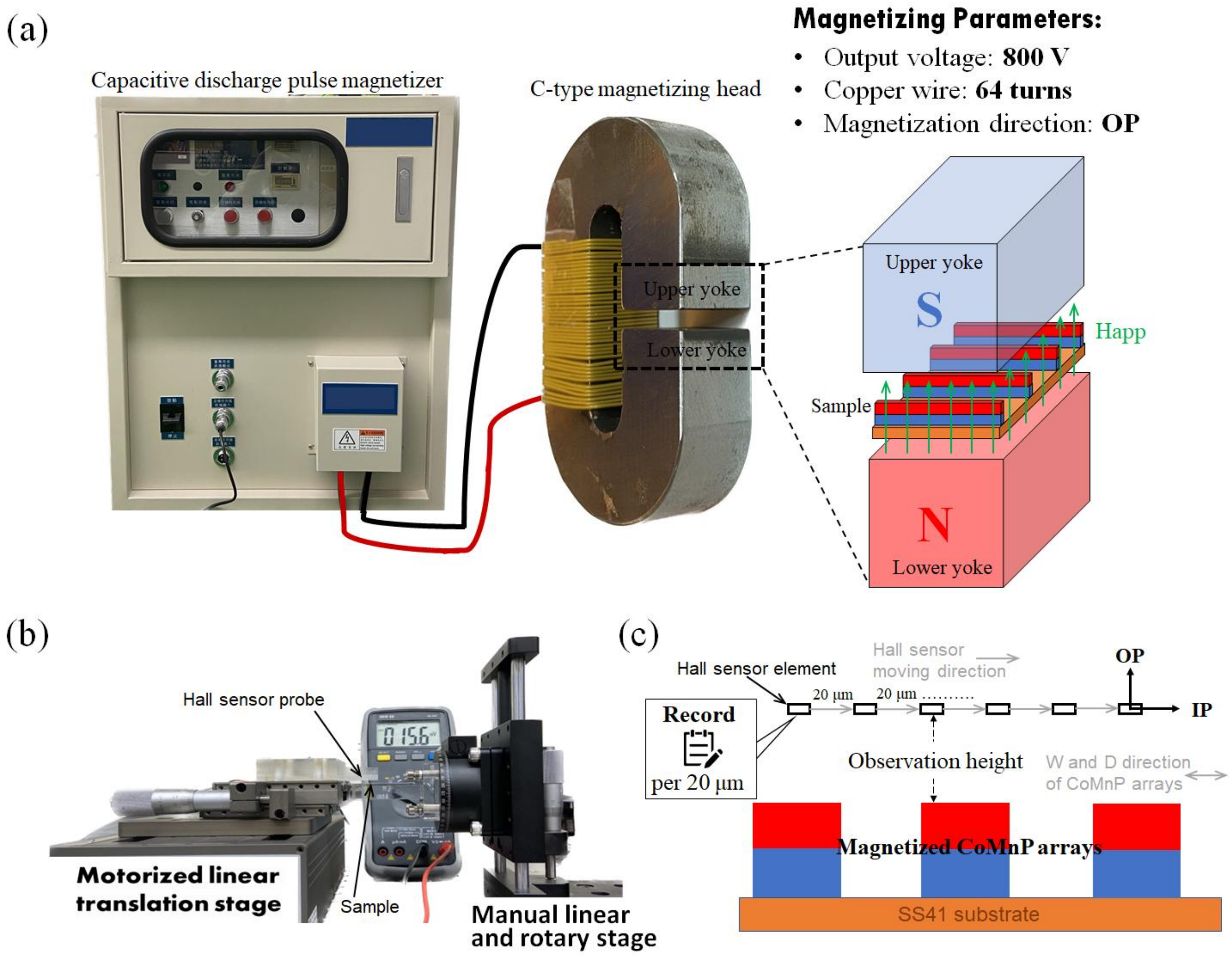

Figure 2. Setups for magnetization and magnetic field measurement: (**a**) Capacitive discharge pulse magnetizer connecting with a C-shaped magnetizing head for magnetization. The scheme on the right indicates the applied magnetic field (Happ) generated from the two yokes, pointing to the OP direction of the sample. Direction of Happ is represented by the green arrows. (**b**) A photograph showing the setup for measuring magnetic flux density as a function of spatial distribution using a Hall sensor. (**c**) A schematic illustration of the magnetic field profile measurement: the magnetic field strength in both the OP and IP directions is measured at 20 μm intervals, in a stepwise manner.

3.2. Measurement of Magnetic Stray Field Profiles

The samples of micro-magnet arrays were placed on a manual stage, allowing fine adjustments along the y- and z-axes and θ rotation. A Hall sensor probe (SENIS F3A, Senis AG, Baar, Switzerland) was mounted on a moving stage controlled by a servo-driven stepper motor (08PTM-50M, Unice E-O Services Inc., Taoyuan City, Taiwan), which offers a minimum step size of 2.5 µm and repeatability of 5 µm. The Hall sensor has spatial resolution values of 10 µm and 30 µm in the in-plane (IP) and out-of-plane (OP) directions, respectively, and can sense in IP and OP directions simultaneously (Figure 2b,c).

During the measurement process, the sample's orientation was first adjusted to align with the primary direction of the Hall probe's sensing axes. The sample position was then adjusted in the z-axis direction to measure the stray field profile at a desired observation height (10 µm, 50 µm and 100 µm) using the method as shown in [10]. Subsequently, the motorized linear stage was programmed to move the Hall probe in increments of 20 µm per step (Figure 2c). With the measured data of stray field strength at each step, the magnetic stray field profile of the patterned CoMnP micro-magnets at a specific observation height can thereby be obtained.

3.3. Materials Characterization

The fabricated samples were inspected using an optical microscope (OM), the Edge 3.0 AM73915MZT model from Dino-Lite, based in New Taipei City, Taiwan. To further analyze the surface morphology of the CoMnP micro-arrays and films, a scanning electron microscope (SEM) was employed. The SEM used was the HITACHI S-4800 model (Hitachi, Tokyo, Japan), equipped with an energy-dispersive spectrometer (EDS) for compositional analysis. To prevent charge accumulation caused by high-energy electrons on the CoMnP surface, a platinum nano-layer was applied via evaporation prior to observation. The SEM operated at a working voltage range of 4 to 10 kV.

A superconducting quantum interference device (SQUID) magnetometer, model MPMS-3 from Quantum Design of the United States, was used to assess the magnetic properties of the CoMnP films by acquiring the hysteresis curves for the ultrasound-assisted electrodeposited samples at room temperature. Both the OP and the IP directions of the CoMnP films were characterized. The measured samples used CoMnP films rather than micro-magnets. The magnetic properties in the OP and IP directions are discussed with the demagnetization factor not being corrected in the present study.

4. Results and Discussion

4.1. Effect of Feature Sizes on the Stray Field Profiles of Micro-Magnet Arrays

Top view inspection results for micro-magnet arrays by SEM can be seen in Figure 3. The light gray stripes are the CoMnP micro-magnets. The periodic grating structures of CoMnP micro-magnets are clear, and the dimensions of width and spacing are almost consistent with the feature sizes designed in Table 1. Figure 3f illustrates an example of direct observation of stray field through placing a magnetic field viewing card on a CoMnP micro-array sample. Periodically alternating polarities are clearly presented.

The Hall probe measurement results of stray field profiles for the CoMnP micro-magnet arrays with a height of 176 µm after magnetization are shown in Figure 4. There are roughly three categories of stray field profiles: triangle wave, sine wave and rectangular wave. When the spacing of micro-magnets is small (i.e., T-W360-D360 and T-W520-D360 samples in Figures 4a and 4d, respectively), the adjacent magnetic polarities interact strongly. Hence, the magnetic stray field lines are mutually squeezing, generating a triangle-shaped stray field profile. Increasing spacing (i.e., T-W360-D520 and T-W360-D680 samples in Figures 4b and 4c, respectively) results in magnetic field shapes evolving towards sine waves along with increasing amplitudes.

In contrast, the OP stray field shape of T-W680-D360 (Figure 4d) is a rectangular wave at the N pole (positive value) and a sinusoidal wave at the S pole (negative value), which is an asymmetrical waveform. This is due to the broadening of the micro-magnets' width, which concentrates the magnetic flux in the CoMnP portion [20]. Note that the IP magnetic stray field presents a saw-tooth-like waveform in Figure 4d. Increasing the observation height makes the OP stray field profile approach sine-wave-like behavior, while the IP stray field profile remains saw-tooth-like.

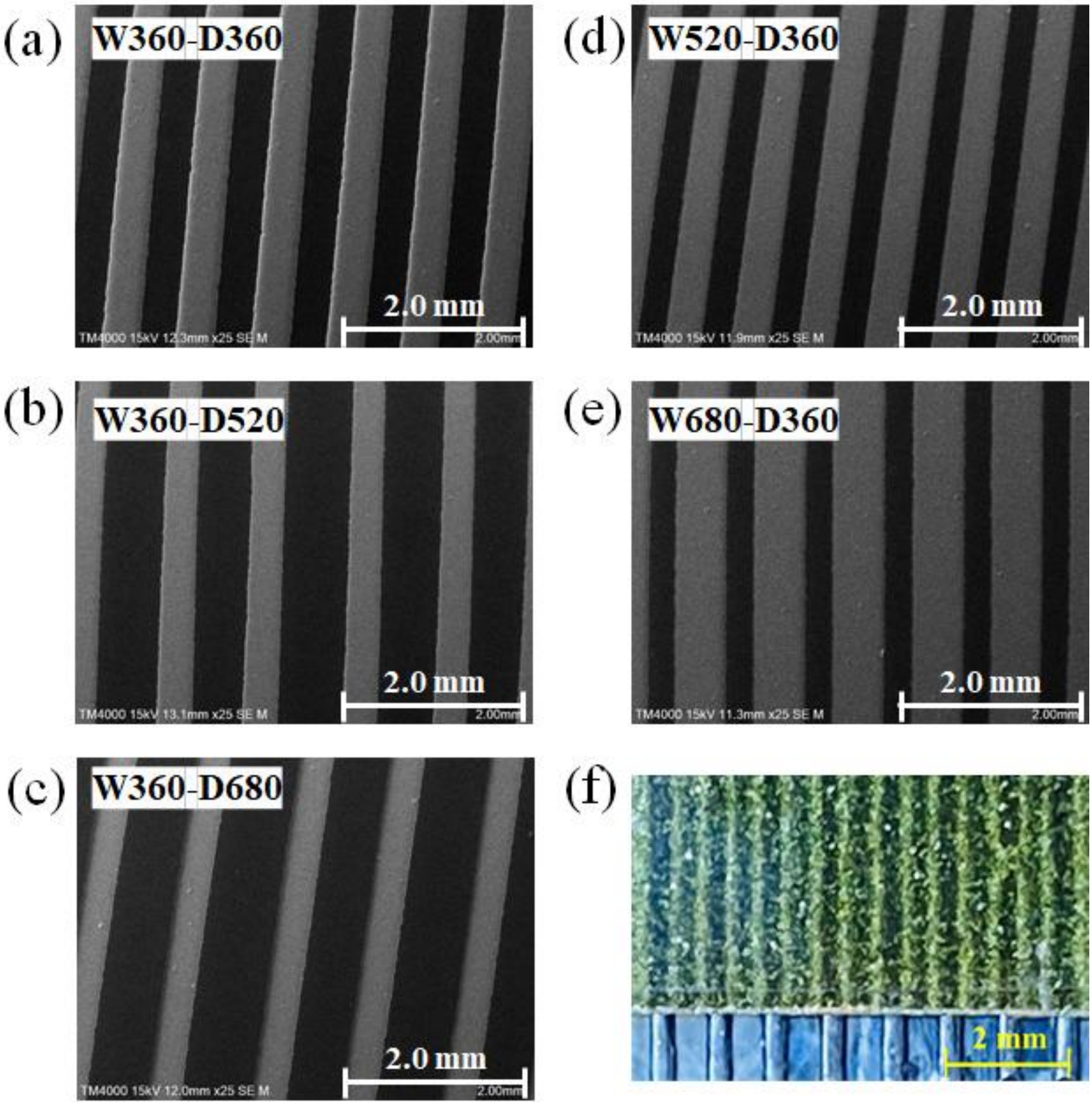

Figure 3. Top view SEM images of the micro-magnet arrays in the format of gratings with different micro-magnet width (W) and spacing (D): (**a**) W360-D360; (**b**) W360-D520; (**c**) W360-D680; (**d**) W520-D360; (**e**) W680-D360. (**f**) Optical image showing a magnetic field viewing card placed on a W680-D360 sample after magnetization. On the bottom of the image a portion of the sample appeared.

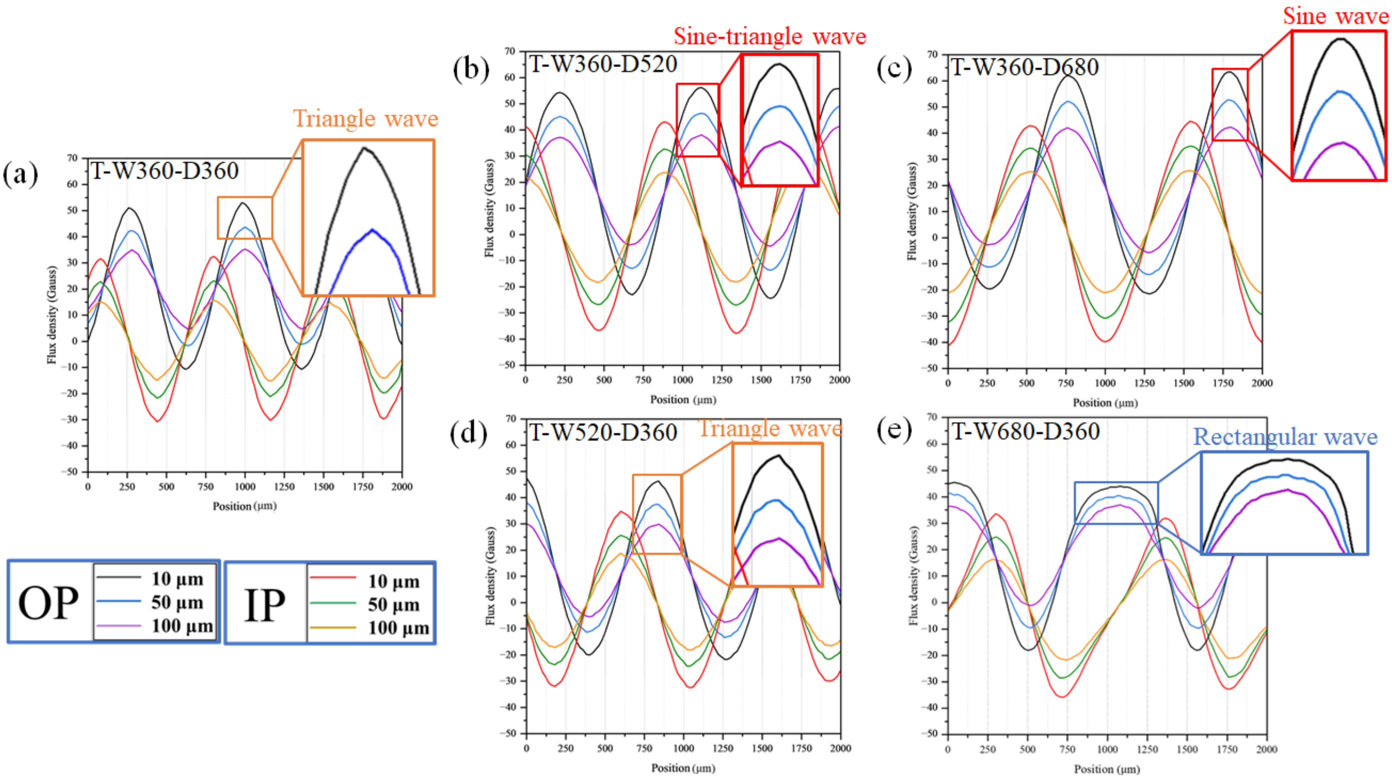

Figure 4. Measurement results of the stray field profiles of (**a**) W360-D360; (**b**) W360-D520; (**c**) W360-D680; (**d**) W520-D360; (**e**) W680-D360 samples with 176 μm height (T-series) micro-magnets. The insets show the enlarged portions of the measurement results.

In addition, the peak-to-peak intensities of the OP and IP stray fields are nearly the same when the observation height is the same. The two directions of magnetic fields have an orthogonal relationship. This indicates that the measurement results are in good agreement with the spatial tensor behavior of distributed magnetic fields for magnetized magnets [35].

Note that the sinusoidal, triangle and rectangular waveforms can be analyzed and quantified through ψ-square tests and/or the fast Fourier transform (FFT) method. A more in-depth study through quantitative analysis for the resultant waveforms of defective stray field profiles is in progress in our research group and will be published in the near future.

For the magnetized CoMnP micro-magnet arrays with a height of 78 μm, the evolution behavior of stray field shape is different (Figure 5). The film-shaped anisotropic effect of the 78 μm height micro-magnets is more significant than the micro-magnet arrays with a height of 176 μm. Thinner micro-magnets are prone to produce sinusoidal stray field waveforms (Figure 5a–c), while on the other side causing a significant reduction in peak-to-peak intensities. This is because the magnetic field intensity is low and the interaction between two adjacent micro-magnets is relatively weakened, so that the magnetic field lines are not significantly interfered with when the spacing is ≥360 μm with a fixed micro-magnet width. However, broadening the width of micro-magnets for F-series abruptly changes the stray field shape to a rectangular waveform (Figure 5d,e). The IP and OP waveform behaviors are similar to the micro-magnets with a height of 176 μm, showing asymmetric polarities and an orthogonal relationship. It is clear that thinning the films of CoMnP alloy for micro-magnets encounters a trade-off between an unfavorable amplitude (i.e., peak-to-peak intensities) and a sine waveform of stray fields. Table 3 summarizes the findings of the magnetic field shape evolution as a function of changing feature sizes for micro-magnet arrays with 78 μm and 176 μm heights.

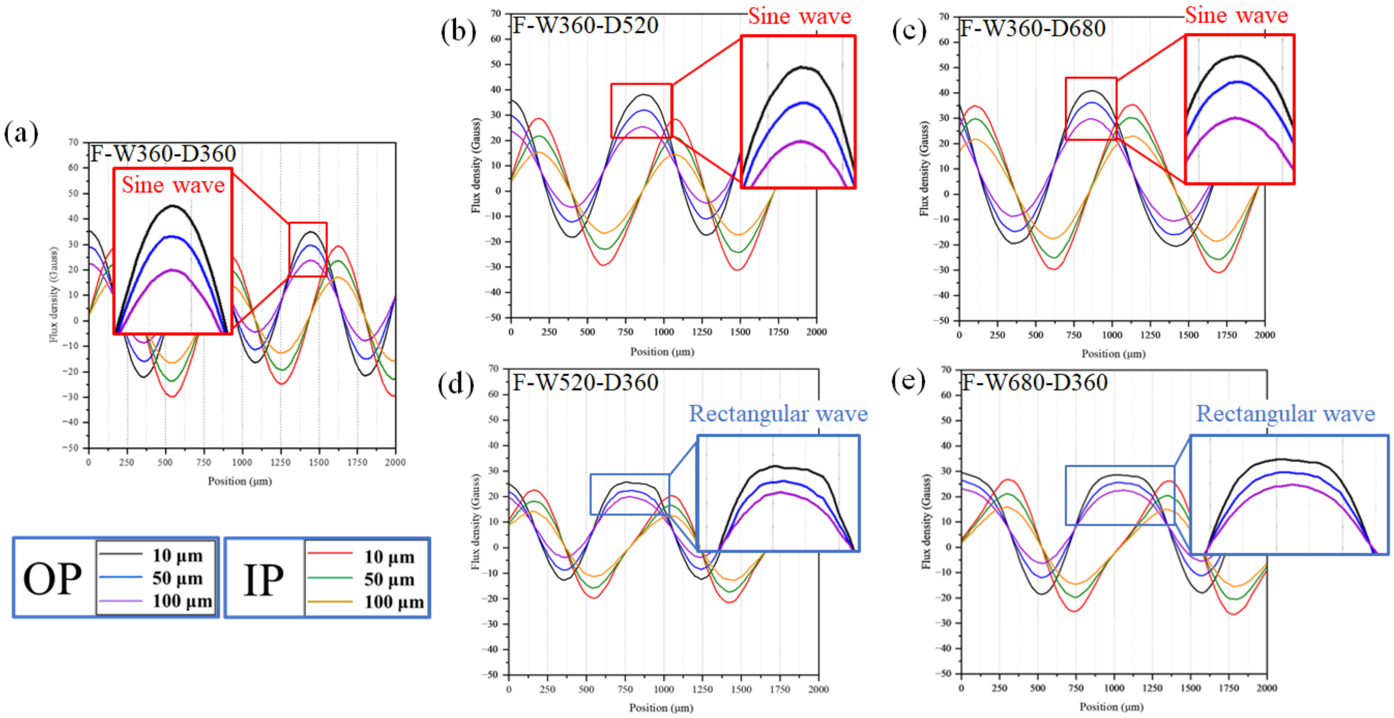

Figure 5. Measurement results of the stray field profiles of (**a**) W360-D360; (**b**) W360-D520; (**c**) W360-D680; (**d**) W520-D360; (**e**) W680-D360 samples with 78 μm height (F-series) micro-magnets. The insets show the enlarged portions of the measurement results.

Table 3. Summary of the magnetic field shape evolution as a function of changing feature sizes for different height of micro-magnet arrays.

Micro-Magnet Height (Series Symbol)	Feature Size	Feature Size Propensity	Field Shape	Height: Width (H/W Ratio)	Height: Spacing (H/D Ratio)
176 μm (T)	W360-D680	Increasing D	Sine	0.49	0.26
	W360-D520	↑	Sine-to-triangle	0.49	0.34
	W360-D360	•	Triangle	0.49	0.49
	W520-D360	↓	Triangle	0.34	0.49
	W680-D360	Increasing W	Rectangle	0.26	0.49
78 μm (F)	W360-D680	Increasing D	Sine	0.22	0.11
	W360-D520	↑	Sine	0.22	0.15
	W360-D360	•	Sine	0.22	0.22
	W520-D360	↓	Rectangle	0.15	0.22
	W680-D360	Increasing W	Rectangle	0.11	0.22

4.2. Effect of Ultrasound Agitation on the Film Quality and Properties

The film thicknesses obtained at different current densities of 5.0 mA/cm^2, 7.5 mA/cm^2, 10.0 mA/cm^2 and 12.5 mA/cm^2 by ultrasound-assisted electrodeposition for 1 h are 3.3 μm, 7.8 μm, 10.6 μm and 14.7 μm, respectively. The film thicknesses obtained at different current densities of 5.0 mA/cm^2, 7.5 mA/cm^2, 10.0 mA/cm^2 and 12.5 mA/cm^2 by air-bubbling electrodeposition for 1 h are 4.1 μm, 5.8 μm, 7.9 μm and 11.7 μm, respectively. At low current density (i.e., 5.0 mA/cm^2), the erosion effect of ultrasound cavitation prevails. Increasing current density leads to an activation effect for reduction reactions and promotes mass transportation for electrolyte species [29]. Therefore, an enhanced deposit rate can be obtained. On the other hand, the co-deposition of CoMnP ternary alloy relies on the reduction potentials of the reactant, chelating and intermediate species in the electrolyte bath. The EDS composition analysis results of the CoMnP hard magnetic films deposited by the two agitation methods indicate that the compositions of the resultant films are nearly identical. The Co, Mn and P contents of the films are 94.0 wt.%, 0.6 wt.% and 5.3 wt.%, respectively. The CoMnP composition is not affected by adopting the two methods of ultrasound-assisted and air-bubbling agitation.

The SEM micrographs of the surface morphologies of the resultant films are shown in Figure 6. There are many micro-cracks and nodules on the surface of the air-bubbling samples, while there are almost no micro-cracks on the surface of the ultrasound-assistance-deposited samples, although the morphologies are slightly rough at high current densities. The reasons for surface micro-cracks are multiple and complex in electrodeposited hard magnetic films. Ultrasound-assisted electrodeposition reduces the formation of micro-cracks through the cavitation effect of ultrasonic waves in the electrolyte solution. The cavitation effect affects the nucleation and growth mechanisms of crystallization for mitigating residual stress and prevents hydrogen atoms from accumulating on the surface for inhibiting hydrogen embrittlement [36–38].

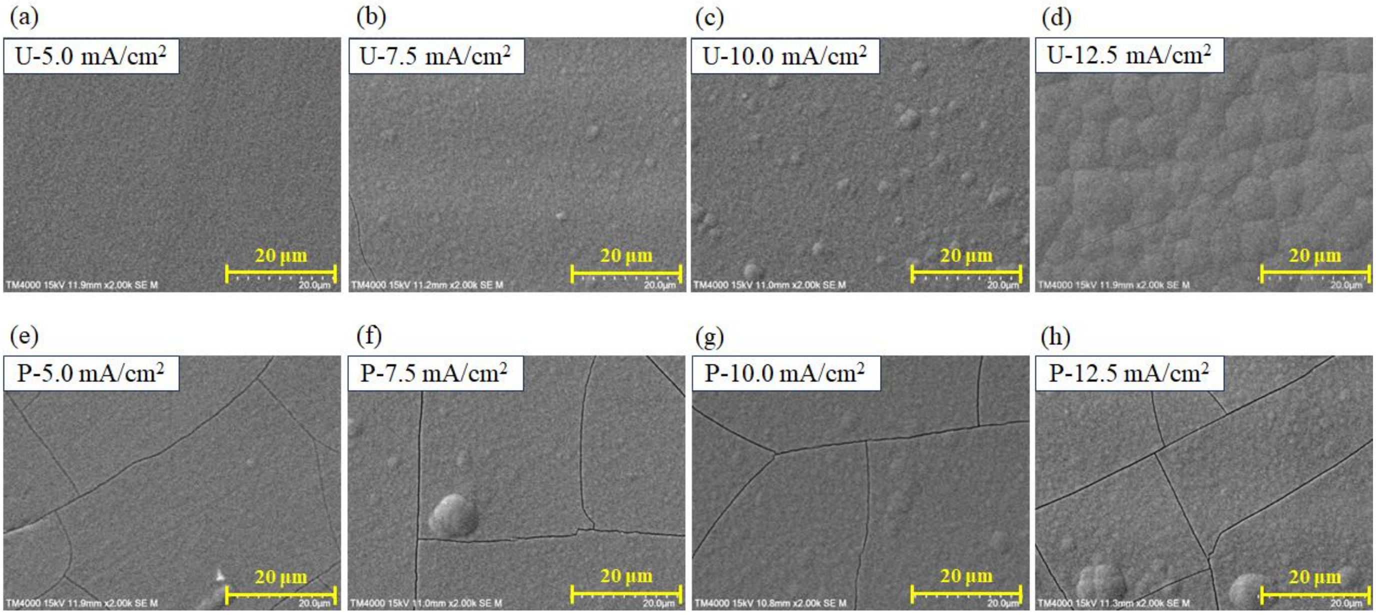

Figure 6. SEM images showing the morphologies of CoMnP hard magnetic films by ultrasound-assisted electrodeposition (denoted as U) at various depositing current density: (**a**) 5.0 mA/cm^2; (**b**) 7.5 mA/cm^2; (**c**) 10.0 mA/cm^2; (**d**) 12.5 mA/cm^2; and by conventional electrodeposition (denoted as P) at various depositing current density: (**e**) 5.0 mA/cm^2; (**f**) 7.5 mA/cm^2; (**g**) 10.0 mA/cm^2; (**h**) 12.5 mA/cm^2.

Figure 7 presents the XRD patterns of the CoMnP hard magnetic films produced by ultrasound-assisted electrodeposition at different current densities. The diffraction peak is very intense with a very low signal-to-noise ratio, which means that the CoMnP hard magnetic films are highly crystalline. In addition, each sample has only one diffraction peak, which indicates that the crystallization of the CoMnP hard magnetic films is textured. Raising current density results in a change in crystalline direction from Co-HCP(110)/Co-FCC(220) texture to Co-HCP(002) texture. The Co-HCP(002) texture can be readily obtained by air-bubbling agitation, and there is no current density dependence behavior. When current density is low, the ultrasonic waves dominate the nucleation and growth mechanisms, because the cavitation effect affects the surface activity of the cathode, altering the kinetic mechanism of ad-atoms motion during depositing [27].

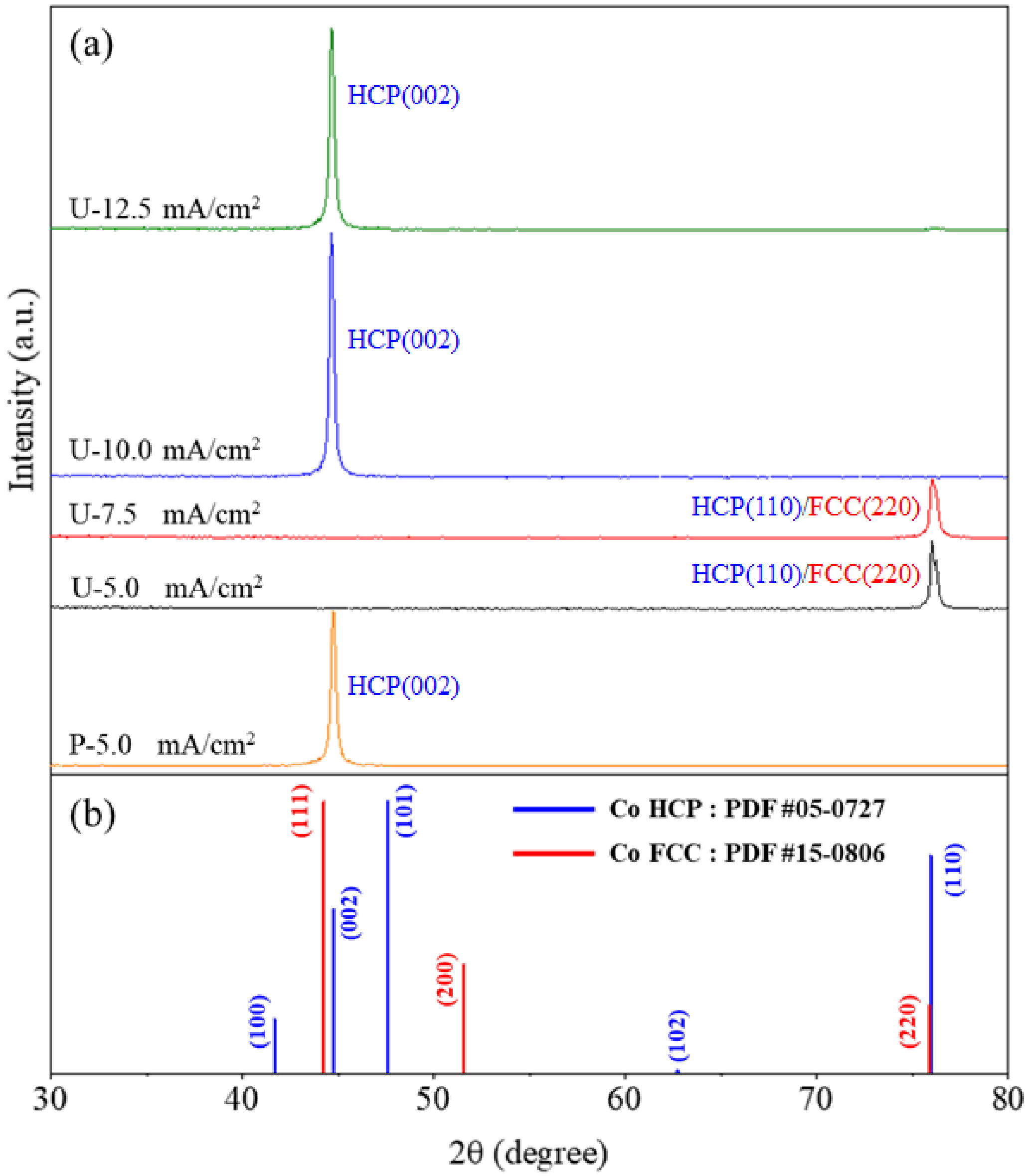

Figure 7. (**a**) X-ray diffraction patterns of CoMnP hard magnetic films by ultrasound-assisted electrodeposition (denoted as U) at various depositing current densities and by conventional electrodeposition (denoted as P) at 5.0 mA/cm^2 current density; (**b**) JCPDS (Joint Committee on Powder Diffraction Standards) card information of crystalline cobalt.

According to the hysteresis curves shown in Figure 8, there is a current density dependence behavior of widening the OP loops when increasing the current density. The results of XRD patterns in Figure 7 explain the measured hysteresis curves of the CoMnP hard magnetic films electrodeposited at different current densities. The CoMnP films with better hard magnetic properties in the IP direction are produced by current densities of 5.0 mA/cm^2 and 7.5 mA/cm^2, which have Co-HCP(110)/Co-FCC(220) diffraction peaks. The CoMnP films with better hard magnetic properties in the OP direction are produced by current densities of 10.0 mA/cm^2 and 12.5 mA/cm^2, which present Co-HCP(002) diffraction peaks [39]. This proves that magneto-crystalline anisotropy due to the *c*-axis easy magnetization direction of HCP Co crystallite dominates the hard magnetic properties of the deposited CoMnP films.

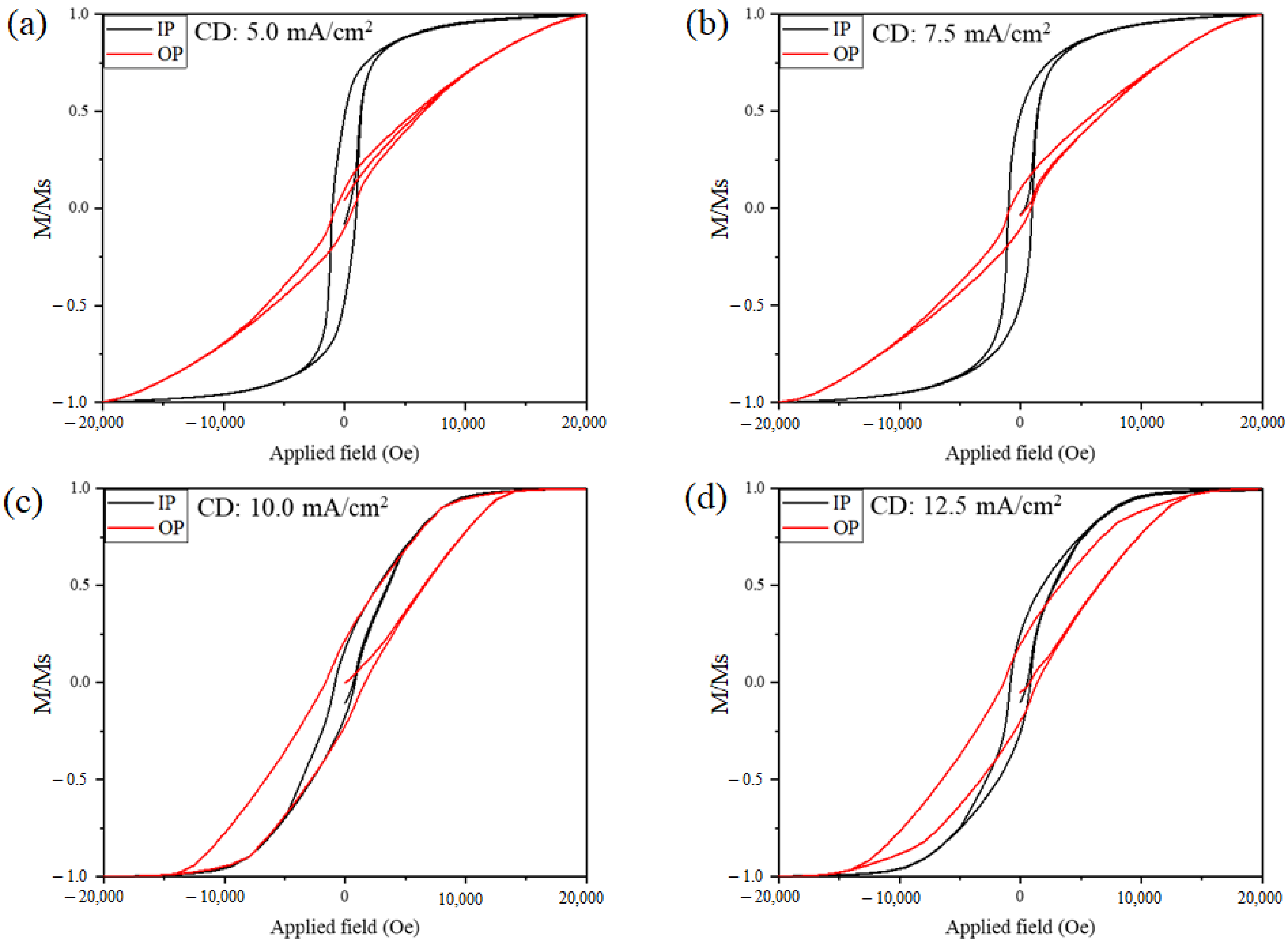

Figure 8. Hysteresis curves (normalized) measured in the OP and IP directions for CoMnP hard magnetic films by ultrasound-assisted electrodeposition under different electrodepositing current density: (**a**) 5.0 mA/cm^2; (**b**) 7.5 mA/cm^2; (**c**) 10.0 mA/cm^2; (**d**) 12.5 mA/cm^2.

Figure 9 is the second quadrant of the B-H curves measured by SQUID in the IP and OP directions. In the OP direction, the CoMnP film electrodeposited with a current density of 10.0 mA/cm^2 has the best hard magnetic properties, with a remanence of 2329 G and a coercivity of 968 Oe. The film deposited with 12.5 mA/cm^2 has a remanence of 2203 G and a coercivity of 882 Oe. In the IP direction, the CoMnP film electrodeposited with a current density of 5.0 mA/cm^2 has the best hard magnetic properties, with a remanence of 8390 G and a coercivity of 952 Oe. The film deposited with 7.5 mA/cm^2 has a remanence of 5176 G and a coercivity of 907 Oe. In the following study for high quality and fine pole pitch micro-magnet arrays using ultrasonic-assisted electrodeposition, a current density of 10.0 mA/cm^2 will be adopted.

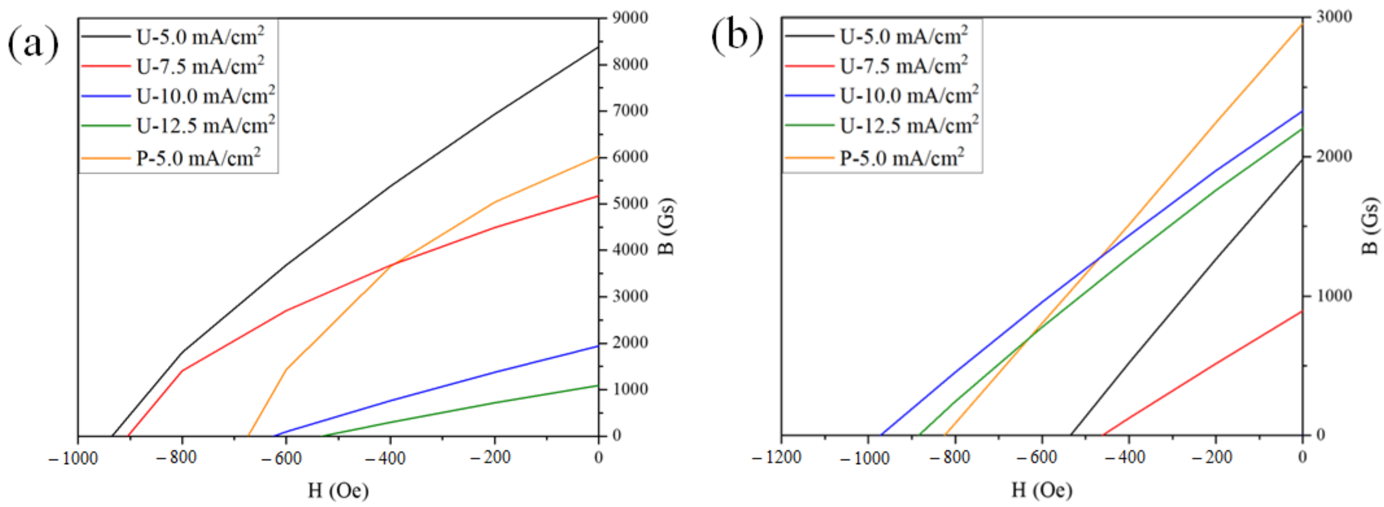

Figure 9. Magnetic measurement results of the second quadrant B-H loops acquired in the (**a**) IP direction; and (**b**) OP direction for samples by ultrasound-assisted electrodeposition (denoted as U) at various depositing current density and by conventional electrodeposition (denoted as P) at 5.0 mA/cm^2 current density.

4.3. High Quality and Fine Pole Pitch Micro-Magnet Arrays

A fine pole pitch M200-D360 mask was adopted for a sequential two-step electrodeposition process of conventional air-bubbling agitation and ultrasound-assisted agitation. The base layer was deposited by conventional air-bubbling agitation with a current density of 5.0 mA/cm^2 for 9 h, and the capping layer was electrodeposited for 1 h with a current density of 10.0 mA/cm^2 by ultrasound-assisted agitation. The height of the resultant W200-D360 micro-magnets is 66 µm.

SEM micrographs of four different magnifications (20×, 100×, 800×, 1500×) were obtained as presented in Figure 10. The feature size is quite consistent with the designed and manufactured mask. At higher magnification, micro-cracks and blisters on the surface of the CoMnP alloy can be observed. However, the areal density of micro-cracks is reduced compared to Figure 6e–h. Several marks and traces of de-bubbling troughs on the surface were found (100× and 800×), which could be caused due to the difficulty of controlling the surface cleanliness and the process continuity during the electrodeposition of laminating. In addition, since the first step of base layer electrodeposition inevitably produces high residual stress, the surface cracking of resultant CoMnP micro-magnets is expected, but the areal density and crack-opening are significantly diminished.

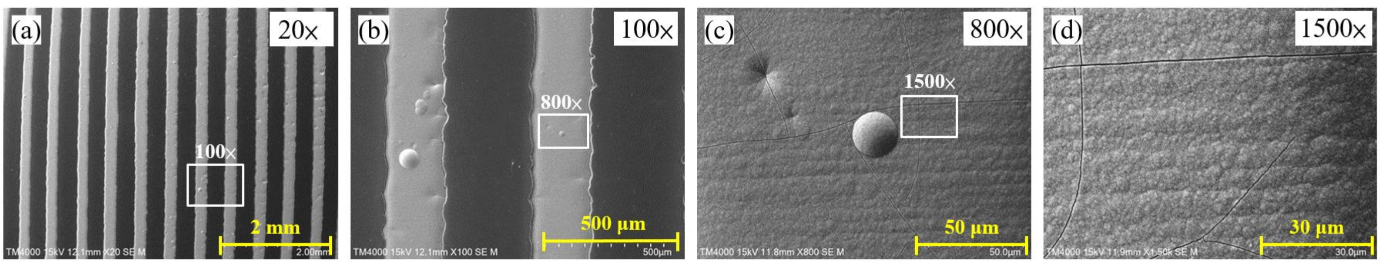

Figure 10. Top view SEM images of the micro-magnet arrays by the combined air-bubbling and ultrasound-assisted agitation electrodeposition, in different magnification: (**a**) 20×; (**b**) 100×; (**c**) 800×; (**d**) 1500×. The zoomed-in areas are denoted by white blocks.

The measured stray field profile of the W200-D360 after magnetization is shown in Figure 11a. The shape of magnetic stray field is sinusoidal, and the orthogonal relationship holds with the IP and OP directions of magnetic fields. However, the overall contour of the field shape is not smooth, indicating that scaling-down the pole pitch encounters more influence of surface micro-defects on the sinusoidal waveform of stray fields. With a reduced volume (i.e., width) of CoMnP alloy, fluctuating magnetization due to surface micro-defects causes the sudden jumps, jagging and discontinuity of the field contour.

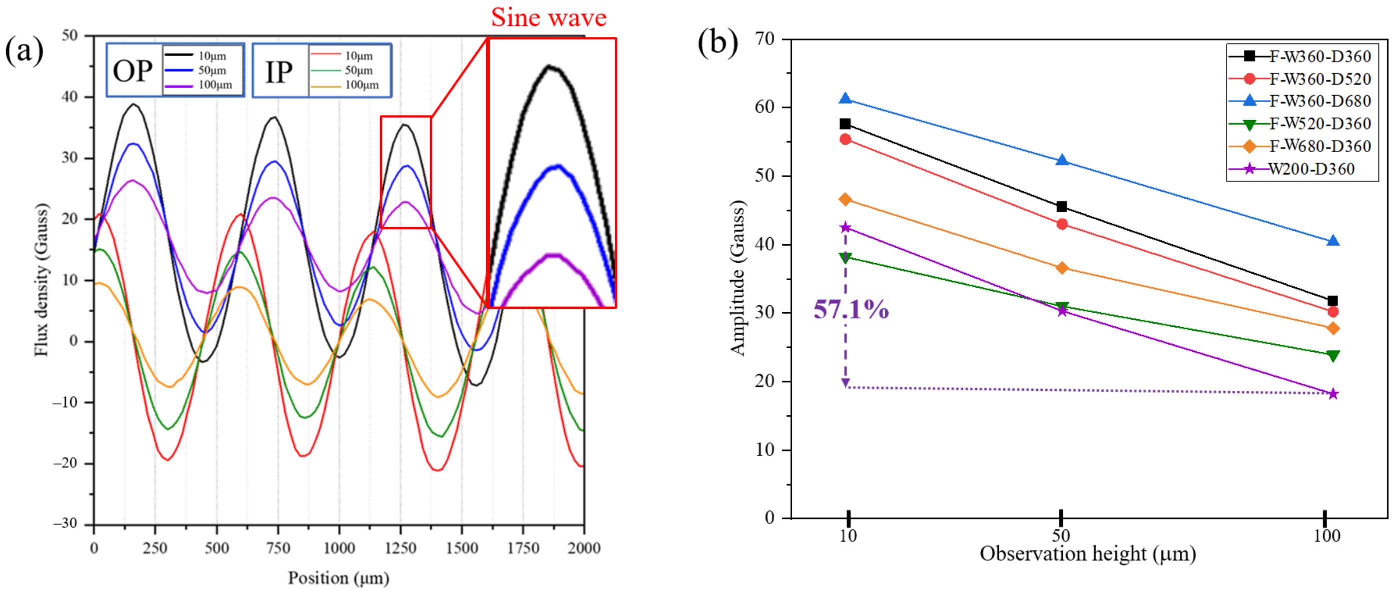

Figure 11. (**a**) Measurement results of the stray field profiles of W200-D360 sample. The inset shows an enlarged portion of the measurement results; (**b**) Amplitude of OP fields as a function of observation height for different feature sizes of micro-magnet arrays.

On the other side, comparison of OP field amplitude with the micro-magnets of F-series is shown in Figure 11a. Although the height of the W200-D360 micro-magnets is slightly smaller (66 μm), the OP field amplitude is comparable to the micro-magnets of F-W520-D360 and F-W680-D3603 when observation height is 10 μm. However, in comparison with F-W360-D360, the OP field amplitude of W200-D360 micro-magnets is significantly weaker at the 10 μm observation height. Moreover, as the observation height increases to 100 μm, the amplitude decrease of the W200-D360 is much greater than that of other micro-magnets with coarser pole pitch. It is clear to see the impact of sacrificing micro-magnet volume for obtaining a finer magnetic pole pitch.

5. Conclusions

This study has developed a recording medium of electrodeposited CoMnP micro-magnets to advance high performance magnetic encoders. Such a novel recording medium of electrodeposited CoMnP micro-magnets can be realized simply through one-time magnetization to form sinusoidal waveforms of magnetic stray fields. There is a relative dimensional relationship among the width, spacing and height of the micro-magnet arrays in order to obtain a perfect sine wave for the stray field. Overly squeezing and heavily interfering of magnetic stray field lines emanated between nearby polarities can result in distorted waveforms. On the other hand, an insufficient height-to-width ratio leads to prevailed film-shaped anisotropy. At the same time, the amplitude of the sinusoidal stray field has to be considered when designing the feature sizes of micro-magnets.

Air-bubbling and ultrasound-assisted agitation methods are effective and efficient for integrating electrodeposition into micro-fabrication processes. In a 37 kHz and 156 W ultrasonic system of CoMnP alloy electrodeposition, the optimal OP hard magnetic properties due to magneto-crystalline anisotropy of Co-HCP(002) texture can be obtained with a current density of 10.0 mA/cm^2. The cavitation effect of ultrasonic waves readily modified the depositing mechanisms, accounting for the current density dependence behavior of the

CoMnP coating texture evolution. The ultrasound-assisted agitation facilitates improved surface quality with reduced microcracks for the electrodeposition of CoMnP alloy. The high-quality hard magnetic films by ultrasound-assisted electrodeposition can be applied in broadened applications such as micro-electromechanical systems (MEMS). Further research work on the reliability and durability of the proposed materials has been preliminarily conducted in our research group for future applications.

Author Contributions: Investigation, formal analysis, G.-H.X. and J.-Y.C.; data curation, visualization, G.-H.X.; methodology, J.-Y.C.; validation, resources, and writing—review and editing, H.-C.H. and C.-C.L.; writing—original draft preparation, J.-Y.C. and C.-C.L.; supervision, H.-C.H. and C.-C.L.; conceptualization, project administration, and funding acquisition, C.-C.L. All authors have read and agreed to the published version of the manuscript.

Funding: This research was funded by the National Science and Technology Council (NSTC), Taiwan, grant numbers 111-2221-E-035-051, 112-2221-E-035-023, 113-2221-E-035-029 and 113-2813-C-035-068-E.

Institutional Review Board Statement: Not applicable.

Informed Consent Statement: Not applicable.

Data Availability Statement: All data that support the findings of this study are included within the article.

Acknowledgments: Appreciation is extended to J.-L. Tsai and K.-W. Lin at the National Chung Hsing University for comprehensive discussion. The authors also wish to thank the Instrumentation Center of National Tsing Hua University, Taiwan, for providing measurement services of hysteresis curves by SQUID (SQUID000300, under the grant number NSTC 112-2740-M-007-001).

Conflicts of Interest: The authors declare no conflicts of interest. The funders had no role in the design of the study; in the collection, analyses, or interpretation of data; in the writing of the manuscript; or in the decision to publish the results.

References

1. Martorana, B.; Carotenuto, G.; Pullini, D.; Zvezdin, K.; La Peruta, G.; Perlo, P.; Nicolais, L. Preparation of plastic ferromagnetic composite materials for magnetic encoders. *Sens. Actuators A Phys.* **2006**, *129*, 176–179. [CrossRef]
2. El Yaagoubi, M.; Haas, S.; Schwegler, D. The magnetic orientation of hard ferrites rubber bonded permanent magnets using the injection moulding. *Sens. Actuators A Phys.* **2021**, *320*, 112571. [CrossRef]
3. Aloui, S.; El Yaagoubi, M.; Münster, B.; Schwegler, D. Influence of the magnetic field during injection molding on the mechanical behavior of thermoplastic copolyester elastomers filled with strontium ferrite. *Sens. Actuators A Phys.* **2023**, *351*, 114177. [CrossRef]
4. El Yaagoubi, M.; Haas, S.; Schwegler, D. Influence of the magnetic field on the alignment degree of the anisotropic strontium ferrites for elastomer bonded magnets. *Polym. Eng. Sci.* **2021**, *61*, 2814–2819. [CrossRef]
5. Bandorf, R.; Gröninger, A.; Ortner, K.; Gerdes, H.; Bräuer, G. Gas flow sputtering for manufacture of high quality hard magnetic films. *Surf. Coat. Technol.* **2017**, *314*, 92–96. [CrossRef]
6. Abrunhosa, S.; Merazzo, K.J.; Costa, T.; Sandig, O.; Franco, F.; Cardoso, S. Reading thin film permanent magnet irregular patterns using magnetoresistive sensors. *Sens. Actuators A Phys.* **2020**, *303*, 111673. [CrossRef]
7. Liu, J.; Xu, X.; Han, G.; Yang, X.; Ai, W.; Hu, W.; Teng, J.; Li, B.; Yu, G. Manipulation of the coercivity of FeCoCr films through artificial defects engineering based on Bi doping. *Appl. Surf. Sci.* **2023**, *609*, 155261. [CrossRef]
8. Liu, J.T.; Xu, X.L.; Feng, G.N.; Yang, X.Y.; Zhao, D.; Zuo, M.G.; Liu, C.Y.; Feng, C.; Liu, S.; Li, B.H.; et al. Coercivity modulation of FeCoCrMoTi films by artificial magnetic phase defects engineering based on multilayer structure. *Acta Mater.* **2023**, *259*, 119241. [CrossRef]
9. Wang, H.C.; Yu, G.H.; Cao, J.L.; Wang, L.J. Electroless plating Co-P films for high performance magnetic rotary encoders. *Sens. Actuators A Phys.* **2011**, *165*, 216–220. [CrossRef]
10. Xu, Z.-H.; Tseng, B.-H.; Chang, C.; Wang, S.-C.; Chin, T.-S.; Sung, C.-K. Grooved multi-pole magnetic gratings for high-resolution positioning systems. *Jpn. J. Appl. Phys.* **2015**, *54*, 06FP01. [CrossRef]
11. Theis, M.; Bill, T.; Knoll, H.; Starke, P.; Saumer, M. Electrochemical deposition of CoP and CoNiP as hard magnetic scales in a position measurement system. *Metals* **2022**, *12*, 235. [CrossRef]
12. Panasyuk, M.I.; Zubar, T.I.; Usovich, T.I.; Tishkevich, D.I.; Kanafyev, O.D.; Fedkin, V.A.; Kotelnikova, A.N.; Trukhanov, S.V.; Michels, D.; Lyakhov, D.; et al. Mechanism of bubbles formation and anomalous phase separation in the CoNiP system. *Sci. Rep.* **2023**, *13*, 5829. [CrossRef]
13. Yanai, T.; Hosohata, R.; Matsumoto, Y.; Yamashita, A.; Nakano, M.; Fukunaga, H. Fe-Co films electroplated from glycine-based plating baths. *IEEE Trans. Magn.* **2023**, *59*, 2001704. [CrossRef]

14. Horkans, J.; Seagle, D.J.; Chang, I.-C.H. Electroplated magnetic media with vertical anisotropy. *J. Electrochem. Soc.* **1990**, *137*, 2056–2061. [CrossRef]
15. Myung, N.V.; Park, D.Y.; Yoo, B.Y.; Sumodjo, P.T.A. Development of electroplated magnetic materials for MEMS. *J. Magn. Magn. Mater.* **2003**, *265*, 189–198. [CrossRef]
16. Chen, Y.-S.; Lin, C.-C.; Chin, T.-S.; Chang, J.-Y.; Sung, C.-K. Residual stress analysis of electrodeposited thick CoMnP monolayers and CoMnP/Cu multilayers. *Surf. Coat. Technol.* **2022**, *434*, 128169. [CrossRef]
17. Chen, Y.-S.; Lin, C.-C.; Chin, T.-S.; Chang, J.-Y.; Sung, C.-K. Residual stress tuned magnetic properties of thick CoMnP/Cu multilayers. *AIP Adv.* **2022**, *12*, 035022. [CrossRef]
18. Cho, H.J.; Bhansali, S.; Ahn, C.H. Electroplated thick permanent magnet arrays with controlled direction of magnetization for MEMS application. *J. Appl. Phys.* **2000**, *87*, 6340–6342. [CrossRef]
19. Wang, Y.; Ewing, J.; Arnold, D.P. Ultra-thick electroplated CoPt magnets for MEMS. *J. Microelectromech. Syst.* **2019**, *28*, 311–320. [CrossRef]
20. Mallick, D.; Paul, K.; Maity, T.; Roy, S. Magnetic performances and switching behavior of Co-rich CoPtP micro-magnets for applications in magnetic MEMS. *J. Appl. Phys.* **2019**, *125*, 023902. [CrossRef]
21. Rhen, F.M.F.; Backen, E.; Coey, J.M.D. Thick-film permanent magnets by membrane electrodeposition. *J. Appl. Phys.* **2005**, *97*, 113908. [CrossRef]
22. Guan, S.; Nelson, B.J. Magnetic composite electroplating for depositing micromagnets. *J. Microelectromech. Syst.* **2006**, *15*, 330–337. [CrossRef]
23. Guan, S.; Nelson, B.J. Pulse-reverse electrodeposited nanograinsized CoNiP thin films and microarrays for MEMS actuators. *J. Electrochem. Soc.* **2005**, *152*, C190. [CrossRef]
24. Huff, M. Recent advances in reactive ion etching and applications of high-aspect-ratio microfabrication. *Micromachines* **2021**, *12*, 991. [CrossRef]
25. Grapes, M.D.; Morris, C.J. Improving the CoNiMnP electrodeposition process using Taguchi design of experiments. *J. Electrochem. Soc.* **2010**, *157*, D642. [CrossRef]
26. Ping, Z.; He, Y.; Gu, C.; Zhang, T.Y. Mechanically assisted electroplating of Ni–P coatings on carbon steel. *Surf. Coat. Technol.* **2008**, *202*, 6023–6028. [CrossRef]
27. Wu, C.-W.; Lin, C.-C.; Chin, T.-S.; Chang, J.-Y.; Sung, C.-K. Effects of cathode rotation and substrate materials on electrodeposited CoMnP thick films. *Mater. Res. Express* **2021**, *8*, 016103. [CrossRef]
28. Tseng, B.-H.; Xu, Z.-H.; Chang, C.; Hsiao, C.-J.; Liu, S.-H.; Hsiao, S.-N.; Sung, C.-K.; Chin, T.-S. Influence of debubbling on crystal structure and magnetic properties of electrodeposited CoNiP layers. *IEEE Trans. Magn.* **2015**, *51*, 1–4. [CrossRef]
29. Lin, C.-C.; Chuang, C.-C.; Li, X.-H.; Chin, T.-S.; Chang, J.-Y.; Sung, C.-K.; Wang, S.-C. Ultrasound-assisted electroless deposition of Co-P hard magnetic films. *Surf. Coat. Technol.* **2020**, *388*, 125577. [CrossRef]
30. Ripka, P.; Mirzaei, M.; Blažek, J. Magnetic position sensors. *Meas. Sci. Technol.* **2021**, *33*, 022002. [CrossRef]
31. Liu, P.-C.; Lin, C.-C. Accuracy variation problem in an incremental magnetic encoder caused by surface flaws of electrodeposited measuring scales. *Measurement* **2024**, *238*, 115366. [CrossRef]
32. Wang, L.; Wu, Y.; Zhang, Y.; Hao, S. Research on angle subdivision method of multi-pole magnetic encoder based on pole number quotient remainder. *IEEE Trans. Magn.* **2021**, *57*, 8002012. [CrossRef]
33. Chen, Z.; Liu, X.; Peng, K.; Yu, Z.; Pu, H. A self-adaptive interpolation method for sinusoidal sensors. *IEEE Trans. Instrum. Meas.* **2020**, *69*, 7675–7682. [CrossRef]
34. Hsiao, H.-S.; Chang, J.-Y. Characterization of signal integrity due to pitch-roll-yaw rotation tolerance in magnetic position sensing systems. *IEEE Trans. Magn.* **2017**, *53*, 3100907. [CrossRef]
35. Takahashi, N. 3D analysis of magnetization distribution magnetized by capacitor-discharge impulse magnetizer. *J. Mater. Process. Technol.* **2001**, *108*, 241–245. [CrossRef]
36. Tudela, I.; Zhang, Y.; Pal, M.; Kerr, I.; Cobley, A.J. Ultrasound-assisted electrodeposition of composite coatings with particles. *Surf. Coat. Technol.* **2014**, *259*, 363–373. [CrossRef]
37. Pan, B.; Yao, Y.; Peng, L.; Zhang, Q.; Yang, Y. Ultrasound-assisted pulse electrodeposition of cobalt films. *Mater. Chem. Phys.* **2020**, *241*, 122395. [CrossRef]
38. Li, B.; Zhang, W. Facile synthesis and electrochemical properties of a novel Ni-B/TiC composite coating via ultrasonic-assisted electrodeposition. *Ultrason. Sonochem.* **2020**, *61*, 104837. [CrossRef]
39. Pattanaik, G.; Kirkwood, D.M.; Xu, X.; Zangari, G. Electrodeposition of hard magnetic films and microstructures. *Electrochim. Acta* **2007**, *52*, 2755–2764. [CrossRef]